Experimental tests of stereological estimates of grain boundary populations

B.W. Reed [a,*], B.L. Adams [b], J.V. Bernier [a], C.M. Hefferan [c], A. Henrie [b], S.F. Li [c], J. Lind [c], R.M. Suter [c], M. Kumar [a]

[a] *Lawrence Livermore National Laboratory, 7000 East Ave., Livermore, CA 94551, USA*
[b] *Department of Mechanical Engineering, Brigham Young University, 435 CTB, Provo, UT 84602, USA*
[c] *Department of Physics, Carnegie Mellon University, 5000 Forbes Ave., Pittsburgh, PA 15213, USA*

Abstract

We present experimental validation of a method for estimating three-dimensional (3-D) relative numerical populations of grain boundaries from measurements of individual two-dimensional (2-D) cross-sections. Such numerical populations are relevant to network topology and the modeling of intergranular failure modes in grain boundary engineered materials, and are distinct from geometrical population measures such as area per volume. We examine 3-D reconstructions of stainless steel and copper, with varying populations of twin-related boundaries, generated by serial-section electron backscatter diffraction and high-energy X-ray diffraction microscopy. We show that 2-D length fractions, 2-D number fractions and 3-D number fractions are all distinct quantities when grain boundary type is correlated with grain boundary size. We also demonstrate that the last quantity may be reliably inferred from the first two, provided the experimental spatial resolution is much finer than the grain size, eliminating the need to use 3-D experimental methods to access at least some information about 3-D network properties. Many of the $\Sigma 3$ boundaries are extremely complex, with highly re-entrant shapes that can intersect a sample plane many times, giving a false impression of multiple separate boundaries.
© 2012 Acta Materialia Inc. Published by Elsevier Ltd. All rights reserved.

Keywords: 3-D characterization; Grain boundary engineering; Electron backscatter diffraction (EBSD); High-energy X-ray diffraction; Twin boundary

1. Introduction

Materials science is greatly concerned with statistical measurements of microstructure, be it the distributions of grain sizes and shapes, crystal orientations, dislocations or minority-phase inclusions. Recently, microstructural studies have been pushing more and more into three dimensions, based on the recognition that two-dimensional (2-D) models can miss a great deal of physically important structure and behavior. Efforts to push into three dimensions have been facilitated by developments in experimental equipment and technique (e.g. serial-section electron backscatter diffraction (EBSD) [1–6] and three-dimensional (3-D) X-ray

techniques [7–9]), as well as improvements in computation, including direct comparison to experiments and/or analysis of experimental data [10–12].

The third dimension often reveals structural information that is difficult or impossible to glean from 2-D measurements or simulations. This is particularly important for behavior dependent on topological connectivity or percolation properties, which can behave markedly differently in different dimensionalities. For example, the notion of a twin-limited microstructure, with a maximal number fraction of $\Sigma 3$ boundaries separating islands of $\Sigma 9$ boundaries in a cubic polycrystal, is only a meaningful concept in two dimensions [13]. Historically, the problem of measuring 3-D properties from 2-D samples led to the long-established field of stereology [14–16]. Certain quantities, such as the volume fraction of a given phase, can be reliably

estimated from certain experimentally accessible quantities, such as the fraction of points randomly chosen on a sample plane that happen to land in that phase. Classical stereology accumulated many such rules, with the virtue of extremely broad applicability and negligible bias, assuming a properly selected sample. Classical stereology forms a starting point for modern efforts to develop 3-D microstructural models that are consistent with statistical measurements [17–20].

Unfortunately, many quantities lack an unbiased classical stereological estimator. This is especially true for quantities that are more topological than geometrical, such as the number density of extended objects with complex shapes, or the sizes of connected grain boundary clusters of certain crystallographic types. While the number density per volume (N_V) of compact shapes may be estimated using the dissector technique [21], this method is not always conveniently available, nor does it apply in a straightforward way when complex, nonconvex shapes are involved. Two objects that appear to be distinct on a pair of nearby planes may be parts of a single, larger object.

The connectivity of specific types of grain boundaries is difficult to measure, lacking even a rough classical stereological analogue. Yet such connectivity significantly affects a material's ability to withstand grain-boundary-related failure and degradation, including thermal coarsening, stress-corrosion cracking and impurity diffusion [22–26]. Theories that describe this behavior [27–30] are based on the number fractions of certain grain boundary types. Number fractions are distinct from the more commonly cited area fractions. When counting number fractions, a single contiguous surface separating two grains counts as one unit, regardless of its area or shape. Thus the number fraction is concerned with relative values of N_V for different boundary types, while the area fraction is concerned with area per volume (A_V), irrespective of how many individual boundaries are involved.

Unfortunately, while A_V is easily derived from the length per area L_A using classical stereology [14,16], N_V is more problematic and cannot be directly estimated from the number per area N_A without independent information about the mean caliper diameter $\overline{D}$, which is difficult to determine without making assumptions about the shapes of the objects being measured. Lacking a dissector, one is left with rough estimates using formulae like $N_V = kN_A^2/N_L$ (N_L being number of intersections per length for a one-dimensional (1-D) sample taken from the 2-D cross-section) [14]. Unfortunately, both $\overline{D}$ and the dimensionless coefficient k in this relation depends on the a priori unknown shape of the object being sampled. Values for $\overline{D}$ and k are tabulated for some simple, compact shapes [14,16], but for complex, re-entrant shapes this method is generally not applied because its biases are too poorly understood.

Such difficulties partly explain why most stereology and 3-D modeling efforts concentrate on more geometrical quantities such as grain size distributions, dislocation den-

sity measured in number per area and A_V for different crystallographic grain boundary types. In this last case, it makes sense to define grain boundary types in terms of the full five macroscopic degrees of freedom, with three defining the misorientation and two describing the local boundary plane normal. Thus the quantities derived in these studies are usually area per volume per differential element in five-dimensional space [31]. Such geometrical quantities are important in understanding, for example, the strength of a material since they are related to the probability that a dislocation will encounter an obstruction when it travels a given distance. The success of the empirical Hall–Petch relation [32] is testament to the value of such analysis.

However, not all material failure and degradation mechanisms are so directly linked to purely geometrical quantities; sometimes topological properties are at least as important. Consider intergranular stress corrosion cracking, a failure mechanism that propagates essentially entirely through grain boundaries as it progresses toward breaking a material in two. If this propagating crack encounters a single boundary, or even a single region within a single boundary, that is exceptionally resistant to cracking (e.g. because it has a crystallographically coherent coincident-site-lattice (CSL) structure), then the entire process can be slowed.

If the material has no spanning 2-D manifold of susceptible boundary area, then the crack must break at least one of the highly resistant boundaries if it is to split the material into two pieces. In this simplified model, each boundary is as strong as its strongest link, and we term a boundary "special" if its misorientation allows such a strong link to exist at some point along its surface. Our results below suggest that such special boundaries may very often contain significant coherent area, despite the convoluted appearance of some of the 2-D cross-sections of the boundary. This definition is convenient for our purposes and is specifically relevant to the class of materials we have considered, which feature complex high-order twinning and highly non-planar boundaries. It allows us to classify boundaries according to their easily measured misorientation, which is roughly constant over the area of the boundary. The other two degrees of freedom (the boundary plane normal) may vary wildly over the same area and may even be discontinuous in the case of a faceted boundary. Our definition of "special" is thus appropriate to a topological description of grain boundary networks. By this we mean that our classification scheme relies on the characteristics that are essentially constant over the entire area of a topologically defined boundary and do not change when the shape of the boundary is continuously varied.

Our approach is distinct from the five-degrees-of-freedom definitions used in more geometrical descriptions [18,31,33–35]. For materials such that most of the boundaries (even those with "special" misorientations) are rather flat, the five-degrees-of-freedom description is likely more appropriate. Of course, both descriptions may be used in

the study of a single material, depending on whether one is interested more in the topological network structure or in the detailed geometrical statistics. A complete understanding of the efficacy of grain boundary engineering likely requires both approaches.

Our rationale for classifying boundaries by their misorientations is based on a mathematical idealization of the relevant failure processes; real crack propagation is not so simple. Once all the nearby boundary area is degraded, stress concentration will ensure that even the most resistant boundary element will eventually fail. Yet this notion of boundary connectivity does seem to bear directly on the stress-corrosion process. Previously [36], we reported that two versions of the same nickel alloy, differing only in grain boundary content and network connectivity, showed both qualitative and quantitative differences in their response to intergranular stress corrosion cracking.

Thus the determination of 3-D topological properties of grain boundary networks is both challenging and important. The first step in such characterization is to determine the 3-D number density N_V of the various boundary types, the relative populations of which are essential to mathematical models of the network connectivity [27–30]. In past work [37] we introduced a method to estimate N_V from a single 2-D cross-section by counting in such a way that two similarly scaling biases roughly canceled each other out. The probability of a boundary intersecting a sample plane is proportional to the square root of its area, as is the mean length $\langle L \rangle$ of the resulting intercept trace, assuming that the boundary is observed. Should some types of boundaries be, on average, much larger than others, then this introduces a bias which can be approximately corrected by asserting $N_V = k' N_A / \langle L \rangle$, k' being a dimensionless shape-dependent factor.

The method's validity rests on some assumptions about the 3-D shapes of the boundaries. We assumed that k' is nearly the same for different types of boundaries – or, at least, that its variations are small enough that our method produces a better estimate than applying no correction at all and assuming $N_V \propto N_A$. Even if k' is not known precisely, if its dependence on grain boundary type is weak, then the residual systematic error for ratios of two N_V values could still be quite low. Our previous work [37] explicitly calculated the relevant shape-dependent constants for elliptical and rectangular shapes, and demonstrated that the variation was relatively small over a reasonably wide range of aspect ratios. The validity for more general shapes, including complex re-entrant shapes that may intersect a sample plane in two or more distinct places, was left as an open question.

Now we present experimental 3-D reconstructions of boundary networks in materials with relatively high densities of special boundaries. Our results show that our bias correction works surprisingly well at estimating the relative N_V of the different boundary types, despite the fact that many of the special boundaries have bizarre, convoluted, re-entrant shapes that seem to violate the assumptions in the derivation. Confirming our original estimates [37], we find that the 3-D number fractions are very different from the 2-D number fractions, such that a $\Sigma 3{:}\Sigma 9$ ratio close to 3:1 in two dimensions is often closer to 2:1 or even 1:1 in three dimensions, affirming the topological importance of $\Sigma 9$s in a 3-D network with a high incidence of complex twinning [13,38]. The method seems to work especially well when the grains are much larger than the scan resolution, suggesting that residual systematic errors are more related to experimental limitations than to the algorithm itself.

2. Methods

Two distinct data sets were analyzed. The first was a serial-section EBSD measurement of stainless steel, with a moderate density of complex twinning yielding $\Sigma 9$ and $\Sigma 27$ boundaries (detailed results in Section 3). The second used non-destructive high-energy diffraction microscopy (HEDM) to reconstruct samples of copper using synchrotron X-ray methods [8,9]. Two copper samples were used – one with a conventional moderately twinned microstructure (the "single-step" processed material from Ref. [39]), and one processed using grain-boundary-engineering techniques ("four-step" processed material [39]) to produce large populations of highly interconnected $\Sigma 3^n$ boundaries. Sample 2-D slices are shown in Figs. 1 and 2. The copper was back-extruded into conical shapes as described previously [39], either in a single step with 60% equivalent plastic strain (conventional) or in four steps with 20% equivalent plastic strain each (engineered). Anneals of 500 °C for 30 min were performed after each step. The conventional and engineered materials had grain sizes of 16 and 28 μm, respectively (counting $\Sigma 3$ boundaries as grain boundaries), and CSL boundary length fractions of 48 and 66%, respectively, as measured by EBSD. Both had nearly random textures. The two copper samples differed markedly in the degree of development of their twin-related domains (TRDs), in a manner typical of the differences between conventional and grain boundary engineered material [30,36,40]. The TRDs in the conventional copper often were either singleton untwinned grains or exhibited a simple back-and-forth twinning pattern. TRDs in the engineered copper frequently exhibited much more complex twinning patterns, yielding convoluted $\Sigma 3$ grain boundaries and much larger populations of $\Sigma 9$ and $\Sigma 27$ boundaries.

The stainless steel (304SS) samples were prepared and analyzed as described in detail in Ref. [41]. The material was heat treated (982 °C for 23.5 h, followed by 675 °C for 8 h), in part to coarsen the grains to improve the ability of scanning EBSD to resolve the grains. Nanoindentations were made at the corners of a 2 mm square to allow coarse registration of each scan. After each 2.3 mm × 2.3 mm EBSD scan at 5 μm resolution, the sample was polished with colloidal silica for ∼5 h at 20 rpm to remove 6.5 ± 2.2 μm of material, as measured by the change in depth of the nanoindentations. The nanoindentations were renewed for each iteration. Once the procedure was established, 41
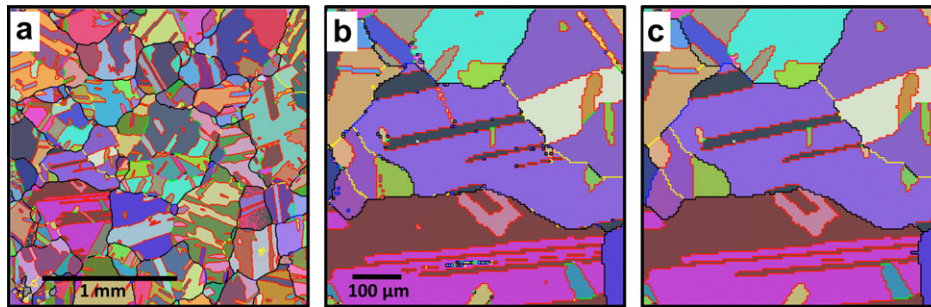
Fig. 1. (a) Wide-area view of a typical slice from the EBSD measurement of steel. Red lines are Σ3 grain boundaries, black lines are random boundaries and other colors code for other CSL boundaries. Background color is grain orientation represented as a linear map from the imaginary parts of the minimum-angle quaternion to (r,g,b) color. This color mapping is one-to-one but discontinuous, accounting for the small number of apparently speckled grains. (b) Close-up of raw data showing small, apparently disconnected twin grains and single-pixel noise at grain boundaries. (c) The same area after recursive small-grain cleanup. (For interpretation of the references to color in this figure legend, the reader is referred to the web version of this article.)
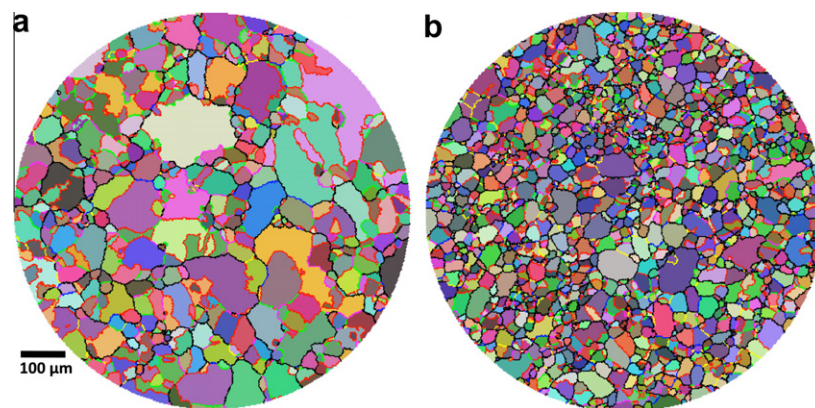

Fig. 2. Typical slices from HEDM of the two copper samples. (a) Grain boundary engineered. (b) Conventionally processed.

such etches were performed, yielding 42 EBSD scans, spanning a depth of 267 μm. The actual measured interlayer spacings were used in the 3-D reconstruction rather than the average interlayer spacing of 6.5 μm. For the data presented herein, this only has a small effect on the 3-D perspective view shown in Fig. 5e and the scatter plots in Fig. 6, while all other results are completely unaffected. The mean interlayer spacing is only slightly larger than the scan spacing of 5 μm; therefore, the probability of failing to see grains that fell between sample layers is not much more than the probability of missing grains between EBSD scan lines. The characteristic sizes of grains and grain boundaries were much larger than the resolution, an average grain boundary trace being 77 μm in length.

The EBSD data sets were filtered to remove single-pixel noise and apparently disconnected twins appearing at the resolution limit of the scan (Fig. 1b and c), using a recursive small-grain-removal algorithm. Grains with apparent areas of 7 pixels ($175 \, \mu m^2$) or less were eliminated, the orientations of all of their pixels being overwritten with those of a representative orientation of the largest neighboring grain. In rare cases, none of the neighboring grains was larger than 7 pixels. In such cases the grain was left untouched and the process was iterated until no sub-threshold grains remained. The cleanup algorithm will likely alter the statis-

tics significantly on a scale below $\sim(175 \, \mu m^2)^{1/2} = 13 \, \mu m$, but should have little effect at larger sizes. The vast majority of the area was dominated by grains much larger than this.

Interlayer registration was performed in two steps, the first using easily identified triple junctions seen in the EBSD scans. We identified 17–20 corresponding triple junctions in each adjacent pair of images, yielding an approximate point-to-point mapping function represented by an ordered pair of second-order polynomials in x and y. χ^2 analysis (Table 1) revealed that an affine transformation was significantly less precise than a second-order transformation, while increasing beyond second order had no significant effect on the residual error, which was reduced to 1.14 pixels RMS across the entire scan area, some of which is surely due to the tilts of the triple junction lines. The inadequacy of the affine transformation suggests that distortions arising, for example, from perspective distortions or nonlinearities in the SEM scanning coils are small yet significant when single-pixel precision is desired.

The scan registration was further refined through a Nelder–Mead simplex direct search using custom code written in MATLAB, varying the 12 fit coefficients of the second-order polynomial to maximize the fraction of overlapping area such that corresponding pixels had nearly matching

Table 1
Justification of the second-order polynomial fit and estimated residual local distortions.

Polynomial degree	1	2	3	4
Mean squared error per DOF (pixels)	1.99 ± 0.16	1.30 ± 0.09	1.23 ± 0.08	1.20 ± 0.08
RMS error (µm)	7.0	5.7	5.6	5.5

For each of the 41 pairs of adjacent layers, 17–20 corresponding pairs of (x, y) locations were hand-chosen from easily recognizable triple junctions. Two-dimensional polynomials of degrees ranging from 1 to 4 were curve fit to this measured distortion. We report the mean squared error per degree of freedom (DOF), including the standard error of the mean, along with the root-mean-square (RMS) residual distortion. Improvements beyond the quadratic model were insignificant.

orientations. After optimization, this fraction was typically about 90%. The mean interlayer misorientation was computed from these points, allowing us to correct the crystallographic reference frame mismatch between the two layers. The accumulated pairwise reference frame shifts (including the polynomial shifts in the scan reference frames and the rotations of the crystallographic reference frames) were collected into a single data structure, such that all 42 layers were represented in a consistent 3-D reference frame with interlayer registration errors of ~1 pixel despite slight nonlinear distortions of the images (Video 1, online).

We had difficulty with the wide range of length scales in the steel's microstructure. While many twin grains were many pixels in width, some were much smaller, comparable to the 5 µm scan resolution. The smallest twins were often disconnected in the discrete scan (Fig. 1b) and, worse yet, were often parallel to similar-sized twins only a few pixels away. Topologically segmenting such a data set can be extremely challenging. Before the small-grain cleanup algorithm, the number fractions were dominated by these small fictitiously disconnected boundaries. In three dimensions, the imperfect registration and the fact that many of the twin planes were close to the sampling plane created a danger of misidentification of one twin with its neighbor. Thus, a simple stitching together of similarly oriented neighboring voxels into 3-D grains did not work well on this data set.

We solved this problem by (i) setting the size cutoff in the recursive small-grain cleanup algorithm to eliminate the vast majority of the fictitiously disconnected boundaries and (ii) developing an anisotropic thresholding method for identifying when two grain boundary traces from neighboring layers should be identified as belonging to the same boundary. This procedure and its associated parameters were developed through trial and error as we watched the performance on common problematic situations. The aim was to develop a simple algorithm that adequately avoided both false positives and false negatives. There are, no doubt, many minor variations on our algorithm that would produce essentially equivalent results. The size, number and aspect ratios of the windows can

Table 2
Grain boundary populations and lengths in 2-D and 3-D for the stainless steel data, including in the last row the stereological estimate of the 3-D number fractions from purely 2-D data.

	Random	Σ3	Σ9	Σ27	Σ1	Other CSL	Total
Traces	$27,654 \pm 166$	$30,939 \pm 176$	8982 ± 95	2739 ± 52	2723 ± 52	3241 ± 57	$76,278 \pm 276$
Boundaries	4211 ± 65	2025 ± 45	1768 ± 42	544 ± 23	785 ± 28	642 ± 25	9975 ± 100
$\langle L \rangle$ (µm)	42.3 ± 0.3	129.2 ± 0.7	35.2 ± 0.4	37.4 ± 0.8	47.2 ± 1.0	49.7 ± 0.9	77.0 ± 0.3
$\langle L \rangle / \langle L_{\text{Random}} \rangle$	1	3.06 ± 0.03	0.83 ± 0.01	0.89 ± 0.02	1.12 ± 0.03	1.18 ± 0.02	1.82 ± 0.01
2-D%L/L_{total}	19.90 ± 0.04	68.05 ± 0.04	5.38 ± 0.02	1.75 ± 0.01	2.19 ± 0.01	2.74 ± 0.02	100
2-D%N/N_{total}	36.3 ± 0.2	40.6 ± 0.2	11.8 ± 0.1	3.6 ± 0.1	3.6 ± 0.1	4.2 ± 0.1	100
Actual 3-D%N/N_{total}	42.2 ± 0.5	20.3 ± 0.4	17.7 ± 0.4	5.5 ± 0.2	7.9 ± 0.3	6.4 ± 0.2	100
Estimated 3-D%N/N_{total}	48.6 ± 0.6	17.8 ± 0.2	19.0 ± 0.4	5.4 ± 0.2	4.3 ± 0.2	4.8 ± 0.2	100

Table 3
As Table 2, for the grain boundary engineered copper.

	Random	Σ3	Σ9	Σ27	Σ1	Other CSL	Total
Traces	$58,483 \pm 242$	$44,454 \pm 211$	$19,357 \pm 139$	$11,968 \pm 109$	3011 ± 55	4626 ± 68	$141,899 \pm 377$
Boundaries	$19,775 \pm 141$	8407 ± 92	6159 ± 78	4111 ± 64	944 ± 31	1532 ± 39	$40,928 \pm 202$
$\langle L \rangle$ (µm)	19.29 ± 0.09	35.34 ± 0.16	20.69 ± 0.16	19.85 ± 0.19	21.2 ± 0.4	20.3 ± 0.3	24.63 ± 0.07
$\langle L \rangle / \langle L_{\text{Random}} \rangle$	1	1.832 ± 0.015	1.073 ± 0.011	1.029 ± 0.012	1.10 ± 0.02	1.052 ± 0.017	1.277 ± 0.010
2-D%L/L_{total}	32.28 ± 0.04	44.95 ± 0.04	11.46 ± 0.03	6.80 ± 0.02	1.82 ± 0.01	2.69 ± 0.01	100
2-D%N/N_{total}	41.22 ± 0.13	31.33 ± 0.12	13.64 ± 0.09	8.43 ± 0.07	2.12 ± 0.04	3.26 ± 0.05	100
Actual 3-D%N/N_{total}	48.32 ± 0.25	20.54 ± 0.20	15.05 ± 0.18	10.04 ± 0.15	2.31 ± 0.07	3.74 ± 0.09	100
Estimated 3-D%N/N_{total}	48.91 ± 0.41	20.30 ± 0.19	15.09 ± 0.22	9.73 ± 0.18	2.29 ± 0.08	3.68 ± 0.11	100

Table 4

As Table 2, for the conventionally processed copper.

	Random	Σ3	Σ9	Σ27	Σ1	Other CSL	Total
Traces	306,727 ± 554	90,379 ± 301	33,749 ± 184	20,768 ± 144	15,225 ± 123	27,326 ± 165	494,174 ± 703
Boundaries	167,887 ± 410	37,551 ± 194	18,660 ± 137	11,938 ± 109	7634 ± 87	15,097 ± 123	258,767 ± 509
$\langle L\rangle$(μm)	13.06 ± 0.03	19.20 ± 0.07	13.39 ± 0.08	12.54 ± 0.10	14.66 ± 0.13	13.22 ± 0.09	14.24 ± 0.02
$\langle L\rangle/\langle L_{Random}\rangle$	1	1.470 ± 0.012	1.026 ± 0.010	0.961 ± 0.010	1.123 ± 0.013	1.013 ± 0.010	1.090 ± 0.008
2-D%L/L_{total}	56.91 ± 0.03	24.66 ± 0.03	6.42 ± 0.02	3.70 ± 0.01	3.17 ± 0.01	5.13 ± 0.01	100
2-D%N/N_{total}	62.07 ± 0.07	18.29 ± 0.05	6.83 ± 0.04	4.20 ± 0.03	3.08 ± 0.02	5.53 ± 0.03	100
Actual 3-D%N/N_{total}	64.88 ± 0.09	14.51 ± 0.07	7.21 ± 0.05	4.61 ± 0.04	2.95 ± 0.03	5.83 ± 0.05	100
Estimated 3-D%N/N_{total}	66.21 ± 0.25	13.27 ± 0.09	7.10 ± 0.08	4.67 ± 0.07	2.93 ± 0.05	5.82 ± 0.07	100

be altered, for example. Fortunately, the most important statistical results (e.g. those to be presented in Tables 2–4) seem to depend little on such details.

Fig. 3 illustrates some of the problematic situations. Each 2-D layer has contiguous paths separating two essentially constant crystal orientations; we will call these paths boundary traces, and they correspond to the intersection of part of a grain boundary with the sample plane. In Fig. 3(a), we see four Σ3 boundaries intersecting two successive sample planes at boundary traces 1, 2, 3 and 4, and 1′, 2′, 3′ and 4′. The interlayer matching algorithm should identify 1 with 1′, 2 with 2′, etc. To avoid misidentifying 1 with 2′, the algorithm must have a sense of direction; it must know that trace 1 has the grain orientation represented as white to its left, with gray to its right, while 2′ has the order reversed. To allow for slight interlayer reference frame errors, we identify orientations from adjacent layers as being equivalent if they are within 5° of one another. This allowed for local grain reference frame orientation distortions while still being quite selective: the probability of two random misorientations both being less than 5° in a cubic crystal is less than 10^{-6}.

The algorithm must have some sense of relative proximity, with nearer traces identified preferentially, so that 1 will be correctly identified with 1′ and not 3′. The algorithm must also be able to handle cases such as in Fig. 3b, with boundaries tilted at a shallow angle with respect to the sample plane. Thus, if there are no compatible traces very close by, the algorithm looks for traces further away. In the case of extremely closely spaced, highly tilted boundaries, the distance from trace 1 to trace 3′ in Fig. 3a may be less than that from trace 1 to trace 1′. Our algorithm, and virtually any simple modification thereof, will misidentify the boundaries in this case. Fortunately, the spacing between sample planes is much less than the typical twin bilayer thickness (e.g. the distance from trace 1 to trace 3), so we expect that this case is rare. Fig. 3c shows a schematic of a common situation in which another sample plane reveals that two apparently distinct boundaries are actually joined in three dimensions. In this case, traces 1 and 2 are part of the same boundary, as revealed by the U-shaped trace in the next layer. The algorithm will label all traces contiguous with either trace 1 or trace 2 as belonging to a single 3-D boundary. Applied to the whole data set, this reveals that many closely spaced parallel twin boundaries appearing in a cross-section, as in Fig. 3a, are in fact parts of a single Σ3 boundary with a very complex 3-D shape, separating two grains interlaced like the fingers of clasped hands.

Boundary traces that satisfy the two criteria (being nearly parallel (not antiparallel) and having compatible grain orientations) must also be spatially near each other in order to be counted as being parts of the same boundary. As illustrated in Fig. 4, we used a hierarchical anisotropic measure of spatial proximity. Centered on each pixel-edge segment of each boundary trace, we placed a rectangular window specifying the maximum range allowed for the center of a similar segment from an adjacent layer. If no compatible segment was found with the smallest window size, the size was increased through a series of three window sizes, allowing more distant segments to be included. In the example, the highlighted segment (solid arrow) has no segments from the next layer (dashed lines) within its first window, but two segments (shown by dashed arrows)
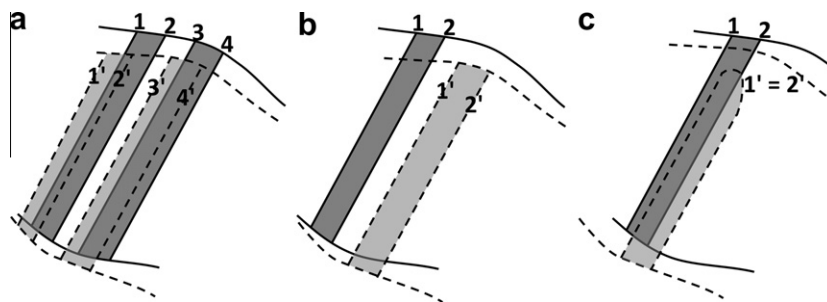

Fig. 3. Illustrating some of the situations encountered by the algorithm that determines when boundary traces in various 2-D cross-sections are parts of the same 3-D boundary. (a) Closely space parallel twins. (b) Twin boundaries tilted at a very shallow angle with respect to the sample planes. (c) A case in which two 2-D boundary traces are revealed to be part of the same boundary in 3-D.
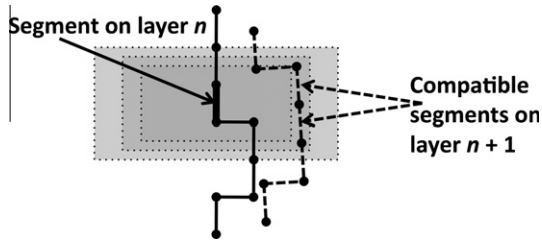
Fig. 4. Schematic of the hierarchical anisotropic thresholding algorithm designed to minimize misidentifications while handling the cases shown in Fig. 3.

within its second window. This was repeated through three successive windows of sizes 20 μm × 10 μm, 30 μm × 10 μm

and 45 μm × 15 μm. The purpose was to allow identification of boundaries that happened to be tilted at glancing angles while avoiding misidentification of closely spaced parallel twins as drawn in Fig. 3a. The window was anisotropic because we wanted to minimize the window area (in order to minimize random false positives) while still capturing the case in Fig. 3b, in which the corresponding traces are separated by fairly large distances in the direction perpendicular to the traces.

Finally, the 3-D boundaries were constructed out of the 2-D boundary traces identified in each layer. If, using the procedure from Fig. 4, any segment from a boundary trace was matched to a segment from a boundary trace in an adjacent layer, then those two boundary traces were deemed
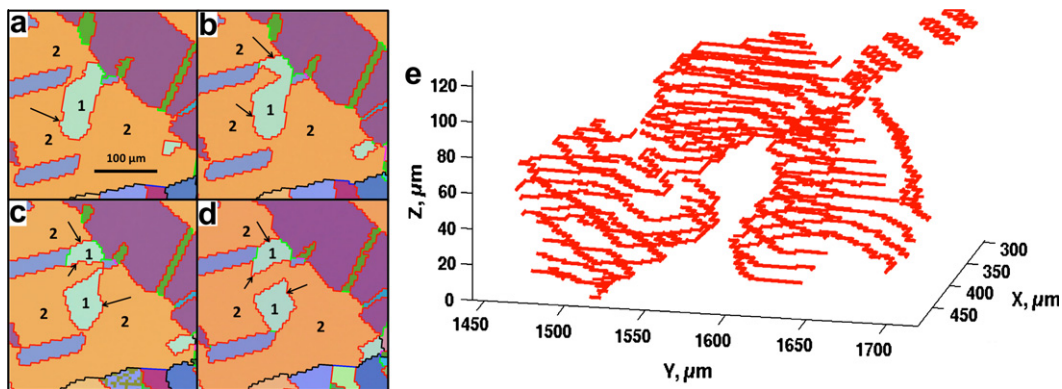

Fig. 5. (a–d) A series of four aligned EBSD images from the steel sample, showing a single Σ3 boundary (arrows) separating only two grains (labeled 1 and 2), despite the appearance of several of the cross-sections. (e) A perspective view of the identified boundary traces defining this single Σ3 boundary.
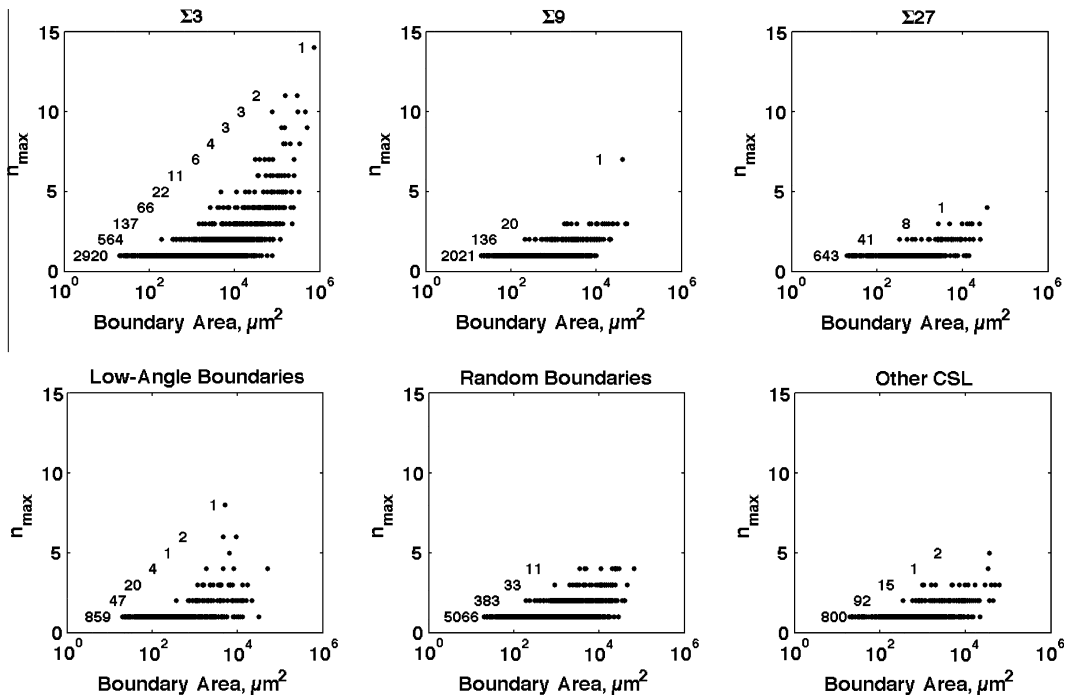

Fig. 6. Scatter plots of total boundary area and n_{max} (the maximum number of appearances of a boundary on a single sample plane) for the six classes of grain boundaries, as determined from the 3-D reconstruction of the steel sample. Numbers indicate histograms of n_{max}.

to be parts of the same 3-D boundary. Once all such pair-wise matches were collected, we constructed the minimal equivalence classes, with each 3-D boundary represented as a set of 2-D boundary traces from a number of different layers.

Because of the situation represented in Fig. 3c, it was very common for single 3-D boundaries to include multiple traces on various single layers. Fig. 5 shows a particularly striking example of this. Fig. 5a highlights (with an arrow) a Σ3 boundary trace separating two grains (regions labeled 1 and 2). In the very next layer (Fig. 5b), the same boundary appears as two boundary traces separating three grains, while in the next layer (Fig. 5c), there are three boundary traces separating what look like four grains, including a twin grain that looks like it is isolated inside the parent grain. In yet another layer (Fig. 5d), this "isolated" grain joins with another, differently oriented twin grain to create a Σ9 boundary (in green). However, a comparison of all four images shows that all of the highlighted boundary traces are parts of a single Σ3 boundary separating just two grains – a medium-sized twin embedded in a much larger grain. Fig. 5e shows a perspective rendering of all of the measured boundary traces from this same boundary, revealing a remarkably complex, highly nonconvex shape with freely mixed coherent (i.e. flat and parallel to the twin's (111) natural plane) and incoherent areas and regions of positive and negative Gaussian curvature, as well as gaps where the twin grain is bounded by Σ9 and other boundaries. We reiterate that this is a single grain boundary. It is not even the entire boundary (it happened to intersect the first layer in the sampled volume), nor is it the only grain boundary to have such a bizarre appearance. We include an animation of the reconstruction (Video 1), in which it is quite easy to find Σ3 boundaries with very unusual shapes by looking closely at various regions and single-stepping forward and backward through the frames.

We also performed 3-D HEDM X-ray reconstructions on 0.9 mm diameter by 0.36 mm cylindrical samples of both copper materials. This produced maps of the crystal orientation at every point in a 3-D volume, with a resolution of 2.8 μm in the x and y directions and 4 μm in the z direction. HEDM is a rotating crystal method applied to polycrystalline materials. It takes advantage of the high-brilliance X-ray source at the Advanced Photon Source. The measurements are done by recording the diffraction patterns produced by a planar, monochromatic X-ray beam incident on a polycrystalline sample rotating on an axis perpendicular to the beam [8]. Conceptually, this is equivalent to performing thousands of rotating single-crystal experiments simultaneously. Different regions in the sample satisfy the Bragg condition at different rotation angles, which, combined with the location of the diffraction spots, defines the crystallographic orientation for each region. The forward modeling method [9] is applied to resolve the crystallographic orientation in each region. The sample space is tessellated into small triangles, assumed to be single crystals or

to have constant orientation. Physically and geometrically compatible diffraction spots are computationally generated for a set of sampled orientations in SO(3) and compared to the experiment. The orientation showing the most similarity between simulated and experimental diffraction patterns is considered the best match. The similarity metric has been the amount of overlap between the simulated and the experimental peaks.

For the HEDM measurements, much of the difficulties encountered with the stainless steel data set did not arise, for two reasons. First, the material itself lacked extremely high-aspect-ratio twin grains ∼1 pixel in thickness, so the size-filtering and anisotropic grain boundary segment matching algorithms were not nearly so critical. Second, by the very nature of the measurement and reconstruction, all of the layers and crystallographic reference frames were already aligned in three dimensions, so the more difficult steps did not need to be performed and the thresholds for proximity and misorientation could be tightened. The identification of 3-D grain boundaries used essentially the same methods as in the steel sample, with a few exceptions. First, all data more than 0.44 mm from the central axis were cut out, owing to the very rapid drop in orientation confidence beyond that radius. This eliminated essentially all of the voxels with unacceptably low confidence and also removed all of the data for surface material that could have been damaged by the sample preparation. Second, the threshold for removing small grains was reduced to a maximum of 3 pixels (or an area of 10.3 μm^2) since the cleanup algorithm was only needed to remove very small ambiguous regions at grain boundaries. Third, since each layer was represented on an equilateral-triangular mesh, the anisotropic edge-matching algorithm needed three distinct edge orientations rather than two (as was the case for the square EBSD scan). Finally, because of the tight tolerances on interlayer registration and the consistently small interlayer spacing, the anisotropic windows were only 1 μm × 1 μm, 5 μm × 5 μm and 20 μm × 10 μm, while the interlayer misorientation threshold was set to 1° instead of the 5° threshold used for the EBSD reconstruction.

3. Results

The boundaries were categorized according to the CSL model, using Brandon's criterion [42] for the maximum angular deviation from exact coincidence. While the general relevance of the CSL model has been debated [30,43,44], there are undoubtedly some CSL misorientations relevant for the structure and properties of face-centered cubic materials. Our ignoring of the unit normal in categorizing the boundaries is consistent with the goals of our general approach, as discussed in the introduction.

The categories we used were: Low-angle boundaries (Σ1, tolerance 15°) (coded yellow in all graphics); Σ3 boundaries, corresponding to the misorientation of a twin, and undoubtedly of high physical importance in these materials (red); Σ9 boundaries, which may or may not have enhanced

properties relative to a random boundary but which are essential for the incorporation of a high $\Sigma 3$ population into a complex, crystallographically consistent network (green); other CSL boundaries from $\Sigma 5$ through $\Sigma 29$, a small population of boundaries, some of which may be somewhat special [41] but most of which probably have rather ordinary physical properties (we tracked these to see if there was any hint of specialness in the populations and size distributions) (blue); and all other boundaries, which we term "random" (black). While some non-CSL boundaries have been identified as having unusual physical properties, we did not consider these in our analysis.

Judging by the observed resistance to corrosion [41], boundaries likely to be "special" in the steel sample include coherent (but not incoherent) $\Sigma 3$ boundaries, low-angle boundaries with misorientations well below $15°$, some $\Sigma 5$, $\Sigma 9$ and $\Sigma 11$ boundaries, and some non-CSL boundaries with no obvious distinguishing crystallographic features.

Statistics describing the results are shown in Tables 2–4. We define a trace as a 1-D intersection of a grain boundary with one of the cross-sections, while a boundary is a set of traces identified as being contiguous in three dimensions. Traces that intersected the edge of the scan region were not counted, nor were boundaries that either intersected the edge of any of the scan regions or were present on the bottom layer. The practice of eliminating boundaries that intersected the bottom layer but allowing those that intersected the top layer is consistent with the rationale behind the dissector method: we want to count the volumetric number density of boundaries, and in essence we are taking the lowest point in each boundary to represent it. If that representative point is in the sample volume, then the boundary is counted. Two-dimensional number fractions for each class of boundaries are defined as the corresponding fraction of the total number of traces, while 2-D length fractions are calculated from the total lengths of all traces, irrespective of how many individual traces are involved. All quoted errors in the tables are derived entirely from $N^{1/2}$ counting statistics.

The differences between the number and length fractions show a correlation between grain boundary size and grain boundary type, i.e. the mean intercept length $\langle L \rangle$ is quite different for different types of boundaries. Thus we estimate the relative 3-D boundary populations by applying the approximate formula $N_V \propto N_A/\langle L \rangle$, assuming the shape-dependent k' factors are roughly independent of boundary type. The last row in each table shows the resulting estimate of N_V for each boundary type, scaled to sum to 100%. This thus provides an estimate of the 3-D number fractions but only uses information present in one 2-D cross-section at a time. Comparison with the next-to-last row (which shows the actual populations as counted in the full 3-D reconstruction) shows favorable results in all three cases – the estimated 3-D populations are, within the error bars, as good or better estimates of the actual 3-D populations than are the 2-D number populations.

For the grain boundary engineered copper sample (Table 3), the agreement is extremely close, with practically all of the residual discrepancy being explainable by the random sampling error. This is also the sample with the largest grains relative to the scan resolution, so that this is the data set that should be least tainted by biases associated with the small-grain-removal algorithm. Thus we suspect that the biases inherent to the $N_V \propto N_A/\langle L \rangle$ estimate are very small, validating our original assertion [37]. This interpretation is supported by the fact that the two data sets with smaller grains (Tables 2 and 4) show similar patterns of residual biases: the last row in each table significantly overestimates the random boundary population and underestimates the $\Sigma 3$ population, while the other boundary types tend to be overestimated if $\langle L \rangle/\langle L_{Random} \rangle$ is small (with a threshold of about 0.9, with some variability from counting statistics) and underestimated if $\langle L \rangle/\langle L_{Random} \rangle$ is large. If our interpretation is correct, then this pattern is created primarily by the limited scan resolution and the small-grain cleanup algorithm.

The results consistently show large $\Sigma 3/\Sigma 9$ ratios exceeding 2.6:1 or even 3:1 in the 2-D numerical populations. After correction, in all cases the random boundary population is much higher, and the $\Sigma 3$ population and $\Sigma 3/\Sigma 9$ ratio much lower (1.1:1, 1.4:1 and 2.0:1), than would be obtained from the 2-D number fractions. Statistical models of the connectivity of highly twinned grain boundary networks [27–30] show strong sensitivity to these population ratios, so it is essential to understand and correct for this bias if we are to understand 3-D network connectivity. Fortunately, the results show that it is not necessary to perform complex 3-D reconstructions to obtain good estimates of these population ratios.

The magnitude of the bias on each boundary type is given by the $\langle L \rangle/\langle L_{Random} \rangle$ rows in Tables 2–4. For the $\Sigma 3$ boundaries, this quantity is invariably significantly greater than 1, and it is the correction associated with the large $\Sigma 3$ boundaries that dominates the corrections to the data. Low-angle ($\Sigma 1$) boundaries are also significantly larger than random boundaries, but the correction associated with this bias is much less dramatic, in part because the $\Sigma 1$ boundaries are much less plentiful than the $\Sigma 3$s. For the other classes ($\Sigma 9$, $\Sigma 27$ and other CSL boundaries), the story is mixed: sometimes these boundaries are significantly smaller than random boundaries, sometimes they are significantly larger and sometimes the difference is immeasurably small. Thus, if we were to suppose that special boundaries tend to have low interface energies and, as a result, larger areas than random boundaries, then we would have to conclude that this analysis of the data reveals little or no evidence that any of these boundaries are special. Yet, at least for the steel samples, corrosion tests indicated that some of the $\Sigma 5$, $\Sigma 9$ and $\Sigma 11$ boundaries were unusually resistant to degradation [41]. Thus statistical tests of specialness through such means as we are presenting should be viewed with some skepticism. $\Sigma 5$ and $\Sigma 11$ boundaries are so rare that such effects could very eas-

ily be lost in the statistics. A more interesting open question is whether these rare sometimes-special boundaries may still play important roles in network connectivity and material performance.

Finally, we consider the correlation between boundary type and boundary shape, which enters into our stereological correction method via the assumption that the average shape-dependent factor k' is roughly independent of boundary type. Fig. 6 shows, for each class of boundaries, the relationship between its estimated area and its tendency to appear multiple times in a single cross-section, using the steel data for this example. We define n_{max} as the maximum number of appearances a specific boundary makes with any sampling plane. For example, a simple non-re-entrant shape that only appears in a single contiguous trace in any single layer will have $n_{max} = 1$, while a boundary that goes up through the layers and reverses direction once to come back down through some of the same layers, so that on some layers it appears in two distinct traces, will have $n_{max} = 2$. Numbers printed on the graph give the histograms of n_{max}. For this graphic we included all of the boundaries, including those that intersected the edges and/or the top and bottom surfaces, so that the largest boundaries would appear. Thus some of the boundary areas and n_{max} values will be underestimates. The boundary areas encompass over four orders of magnitude and are significantly correlated with n_{max}. But more interesting is the variation in the distribution of n_{max} with boundary type. The vast majority of the highly re-entrant boundaries are $\Sigma 3$s, including one outstanding example that makes no less than 14 distinct appearances on a single layer. This supports our claim that highly convoluted $\Sigma 3$ boundaries are quite common in this data set, and that the boundary shown in Fig. 5, far from being a lone outlier, is just one of dozens of boundaries that are at least as complex. It is quite common, as we have said, for closely spaced parallel twin boundaries (shown schematically in Fig. 3a) to in fact be parts of the same 3-D boundary, being demonstrably connected in one or more layers. For the non-$\Sigma 3$ boundary types, typically only ∼1–2% (or close to 3% for the low-angle boundaries) of the boundaries even have an n_{max} of 3 or more, compared to 6.8% of the $\Sigma 3$ boundaries. Even though 78% of the $\Sigma 3$ boundaries have $n_{max} = 1$ and thus have relatively simple 3-D shapes, as the boundary area exceeds a few thousand square micrometers, these "simple" boundaries become less and less representative, and the complex re-entrant shapes take over entirely for boundaries larger than ∼10^5 μm^2.

This has some interesting implications. First, it is clear that simple models based on (for example) Voronoi-tessellation initial conditions and/or purely curvature-driven boundary evolution would have an extremely hard time accounting for such boundary shapes. It is hard to envision how boundaries like those shown in Fig. 5 could represent free energy minima except in a very local sense, and accounting for their shapes would have to incorporate some fairly complex physics (e.g. pinning sites or extreme defect density or stress gradients that cannot be easily seen by

the EBSD or HEDM methods, or dominance by kinetic factors such as the extremely low mobility of coherent sections of a $\Sigma 3$ boundary, such that all such boundaries are essentially frozen in metastable states). This provides a cautionary tale for efforts to derive grain boundary energies from boundary area populations or triple-junction angular distributions. While such approaches undoubtedly have much validity and have produced very good results [45,46], there may be some materials and some boundary types that will prove problematic. To address the question, we are developing studies of dihedral angle distributions, and their evolution under annealing, for different triple junction types.

Second, our samples clearly violate one of the assumptions in the derivation of our stereological correction method. Boundary shape is definitely correlated with boundary type. So why does the correction work as well as it does? Our original derivation [37] included this assumption as a sufficient condition, but we have never addressed the conditions necessary for our algorithm to produce good estimates of the 3-D number fractions. Perhaps the fact that over 93% of the $\Sigma 3$ boundaries have n_{max} values of only 1 or 2 is responsible? While the highly complex, multiply re-entrant boundaries are very striking, they are not very plentiful in comparison to the entire sample size. Or perhaps the method is more robust than we had first envisioned, for a boundary that appears multiple times on one layer, and would thereby be overcounted in a 2-D survey of numerical populations in which it appears, is also less likely to intersect a random sample plane than would be a flat boundary of the same area – which would introduce an undercounting bias of similar magnitude. This concept could be tested with Monte Carlo calculations involving a variety of complex boundary shapes.

4. Conclusions

We have presented reconstructions of two distinct material compositions (stainless steel and copper), one with two different processing histories (conventional and grain boundary engineered), using two different experimental methods (serial-section EBSD and HEDM). We have introduced an algorithm designed for robust identification of boundary traces between sample planes in the face of such difficulties as nonlinear distortions, closely spaced parallel twins and grains with widths comparable to the scan resolution. The resulting reconstructions reveal complex networks of grain boundaries, including some grain boundaries (especially $\Sigma 3$s) with extremely complicated 3-D shapes. These boundaries dramatically violate some common assumptions – that grains are generally convex, roughly equiaxed and simply connected, that individual grain boundaries are simply connected and nearly planar, and that boundary traces seen in 2-D cross-sections usually represent distinct boundaries. While such anomalous boundaries are numerically not very common, they are typically so large that they still represent quite a substantial fraction of the total grain boundary area.

We also find that numerical boundary populations taken from 2-D cross-sections can be very different from the actual 3-D populations. Fortunately, a simple algorithm [37] can correct the great majority of this bias, and the results suggest that the residual bias owes more to small-grain cleanup algorithms than to biases in the algorithm itself. The correction has very significant effects on the special boundary fraction, as well as on the $\Sigma3/\Sigma9$ ratio, both of which are important parameters in the statistical modeling of grain boundary engineered networks [27–30]. Now that our stereological algorithm is validated against 3-D data, it can now be used to improve our understanding of 3-D network statistics in grain boundary engineered materials, taking advantage of the enormous amount of relevant 2-D data (EBSD and otherwise) accumulated over the past decade. For some statistical applications, 3-D experimental methods are not necessary.

Yet the results also suggest network analysis methods that fundamentally cannot be done using isolated 2-D cross-sections and require fully 3-D methods. The scatter plots in Fig. 6, for example, could not have been produced from 2-D data. More generally, the relative N_V populations yielded by the stereological algorithm tell us little about the connectivity of the network, apart from the role that these values play in statistical theories. The 3-D number densities and length distributions of particular kinds of triple junction lines, for example $\Sigma3$–$\Sigma3$–$\Sigma9$, may be very important, as may be the distributions of contiguous clusters of special and random boundaries. Fully 3-D data sets such as ours can be used to analyze such properties while revealing the true structure of grain boundary networks within twin-related domains [47], clarifying the role of complex twinning in producing the well developed networks of $\Sigma3^n$ boundaries that seem to be essential for the performance of grain boundary engineered materials. Such analysis on our existing data would go well beyond the scope of the present paper and will be left to future publications.

Three-dimensional data can also reveal the spatial correlations of different boundary types and the degree of complexity of the interconnections among special boundaries. The $\Sigma3$ boundary shown in Fig. 5 freely intermixes coherent and incoherent regions in the same boundary and shares triple junctions with at least seven distinct $\Sigma9$ boundaries (and probably more; as we noted, the boundary continues beyond the end of the sampled region). Theoretical models of grain boundary engineered networks have generally been simplified to the point where such boundaries are simply not considered. Now, with experimental data showing what the boundary networks really look like in 3-D, the modeling community has the empirical justification needed to push the models to much higher levels of complexity and realism.

Acknowledgements

Appendix A. Supplementary data

Supplementary data associated with this article can be found, in the online version, at doi:10.1016/j.actamat.2012.02.005.

References

[1] Groeber M, Haley B, Uchic M, Ghosh S. Mater Process Design: Model Simulat Appl – Pts 1 and 2 2004;712:1712.
[2] Lee SB, Rollett AD, Rohrer GS. Recrystal Grain Growth III – Pts 1 and 2 2007;558–559:915.
[3] Zaefferer S, Wright SI, Raabe D. Metall Mater Trans A 2008;39A:374.
[4] Uchic MD, Groeber MA, Rollett AD. JOM 2011;63:25.
[5] Rollett AD, Lee SB, Campman R, Rohrer GS. Annu Rev Mater Res 2007;37:627.
[6] Rohrer GS, Li J, Lee S, Rollett AD, Groeber M, Uchic MD. Mater Sci Tech – Lond 2010;26:661.
[7] Liu WJ, Ice GE, Larson BC, Yang WG, Tischler JZ. Ultramicroscopy 2005;103:199.
[8] Poulsen HF, Nielsen SF, Lauridsen EM, Schmidt S, Suter RM, Lienert U, et al. J Appl Crystallogr 2001;34:751.
[9] Suter RM, Hennessy D, Xiao C, Lienert U. Rev Sci Instrum 2006;77:123905.
[10] Zaafarani N, Raabe D, Singh RN, Roters F, Zaefferer S. Acta Mater 2006;54:1863.
[11] Cayron C, Artaud B, Briottet L. Mater Charact 2006;57:386.
[12] Thornton K, Poulsen HF. MRS Bull 2008;33:587.
[13] Gertsman VY, Reed BW. Z Metallkd 2005;96:1106.
[14] Underwood EE. Quantitative stereology. New York: Addison-Wesley; 1970.
[15] Mayhew TM. J Anat 1979;129:95.
[16] Russ JC, Dehoff RT. Practical stereology. New York: Kluwer; 2000.
[17] Bunge HJ, Schwarzer RA. Adv Eng Mater 2001;3:25.
[18] Khorashadizadeh A, Raabe D, Zaefferer S, Rohrer GS, Rollett AD, Winning M. Adv Eng Mater 2011;13:237.
[19] Groeber M, Ghosh S, Uchic MD, Dimiduk DM. Acta Mater 2008;56:1257.
[20] Frary M. Scripta Mater 2007;57:205.
[21] Sterio DC. J Microsc – Oxford 1984;134:127.
[22] Watanabe T, Tsurekawa S. Acta Mater 1999;47:4171.
[23] Tsurekawa S, Watanabe T, Tamari N. Adv Fract Failure Prevent – Pts 1 and 2 2004;261–263:999.
[24] Was GS, Alexandreanu B, Andresen P, Kumar M. Mater Res Soc Symp Proc 2004;819:87.
[25] Schwartz AJ, King WE, Kumar M. Scripta Mater 2006;54:963.
[26] Bechtle S, Kumar M, Somerday BP, Launey ME, Ritchie RO. Acta Mater 2009;57:4148.
[27] Gertsman VY. Acta Crystallogr A 2001;57:649.

[28] Schuh CA, Minich RW, Kumar M. Philos Mag 2003;83:711.
[29] Frary M, Schuh CA. Phys Rev B 2004;69:134115.
[30] Reed BW. Schuh CA. In: Schwartz AJ, Kumar M, Adams BL, Field DP, editors. Electron backscatter diffraction in materials science. New York: Springer; 2009. p. 201.
[31] Morawiec A. J Appl Crystallogr 2009;42:783.
[32] Hall EO. Proc Phys Soc Lond Sect B 1951;64:747.
[33] Kim CS, Rollett AD, Rohrer GS. Scripta Mater 2006;54:1005.
[34] Saylor DM, El-Dasher BS, Adams BL, Rohrer GS. Metall Mater Trans A 2004;35A:1981.
[35] Larsen RJ, Adams BL. Metall Mater Trans A 2004;35A:1991.
[36] Reed BW, Kumar M, Minich RW, Rudd RE. Acta Mater 2008;56:3278.
[37] Reed BW, Kumar M. MRS Proc 2004;819:283.
[38] Randle V, Coleman M, Waterton M. Metall Mater Trans A 2011;42A:582.
[39] Blobaum KJM, Stolken JS, Kumar M. MRS Proc 2004;819:51.
[40] Kumar M, Schwartz AJ, King WE. Acta Mater 2002;50:2599.
[41] Henrie AJM. PhD Thesis. Brigham Young University, Provo, UT; 2004, p. 79.
[42] Brandon DG. Acta Metall 1966;14:1479.
[43] Lejcek P, Paidar V. Mater Sci Tech – Lond 2005;21:393.
[44] Randle V. Scripta Mater 2006;54:1011.
[45] Smith CS. Trans Am Inst Min Metall Eng 1948;175:15.
[46] Rohrer GS, Holm EA, Rollett AD, Foiles SM, Li J, Olmsted DL. Acta Mater 2010;58:5063.
[47] Reed BW, Kumar M. Scripta Mater 2006;54:1029.